Interfacial control of SrTiO₃/Si(001) epitaxy and its effect on physical and optical properties

Tsang-Hsuan Wang[1,2,*], Robert Gehlhaar[1], Thierry Conard[1], Paola Favia[1], Jan Genoe[1,2], Clement Merckling[1,3]

1: Imec, Kapeldreef 75, B-3001 Leuven, Belgium

2: ESAT Department, KU Leuven, Kasteelpark Arenberg 10, B-3001 Leuven, Belgium

3: Department of Materials Engineering (MTM), KU Leuven, Kasteelpark Arenberg 44, B-3001 Leuven, Belgium

*e-mail: tsang.hsuan.wang@imec.be

Key words

A1. Interfaces; A1. Reflection high energy electron diffraction; A3. Molecular beam epitaxy; B1. Perovskites; B1. Titanium compounds

Abstract

The direct heteroepitaxy of strontium titanate (SrTiO₃, STO) oxide on Si(001) substrate is an important step to integrate other functional perovskite oxides onto large scale wafers. In this study, we focused on the SrO interfacial layer in function of molecular oxygen gas exposure amount prior to the STO growth. The various formed interfaces showed large impact on the subsequent STO growth, including crystal quality and stoichiometry. The chemical binding states showed that the formation of thick SiOₓ interfacial layer was strongly correlated with the molecular oxygen exposure amount. More interestingly, the film stoichiometry is also

strongly affected with overexposure, which resulted in optical properties degradation of the STO films. The STO optical constants, extracted from the spectroscopic ellipsometry (SE), exhibit obvious differences between crystalline and amorphous samples. Finally, post-deposition annealing was used to reduce the optical extinction, which is of primary importance for photonic applications.

Introduction

Strontium titanate (SrTiO$_3$, STO) is a widely studied perovskite oxide material which showed potential applications in various electronics fields[1,2]. STO is reported to have large dielectric constant, high breakdown strength, and tunable conductivity with doping, making this material attractive for energy storage and memory applications[3,4] .

Other than applications in electronics, STO can also act as a perfect template buffer layer for other perovskite oxides materials to be integrated on Si wafer. Due to its good thermodynamic stability with Si[5], the STO layer can be directly grown on Si(001) substrate by molecular beam epitaxy (MBE) with well controlled interface and stoichiometry[6,7]. By using STO as buffer layer, various single crystalline functional perovskite oxides can be monolithically integrated onto Si, preserving the desired physical properties, and obtaining the compatibility with industry.

Barium titanate (BaTiO$_3$, BTO), for example, is a ferroelectric material that also presents large Pockels coefficients, which makes it very attractive for integrated photonic devices like high-speed modulators. With STO as buffer layer, epitaxial BTO films are demonstrated with good crystallinity and a large electro-optical effect[8,9]. On the contrary to the widely investigated BTO optical properties, the intrinsic optical performances of ultra-thin STO layers on Si(001) still require further investigations. The optical properties of epitaxial STO were most explored by using transparent oxide substrates, such as KTaO$_3$ and LaAlO$_3$[10,11], while the ones integrated on Si were of larger thickness[12]. In this study, we investigated the optical properties of thin STO films, which showed to be largely affected by the interface control. The crystallinity differences of these layers resulted in different dispersions of the refractive index both in real and imaginary parts.

Experimental

The 4-nm STO films were grown on 8-inch Si(001) substrate in a Riber 49 200mm molecular beam epitaxy (MBE) tool. The strontium was evaporated from an effusion cell, and the titanium molecular beam was produced by an electron beam evaporator. Molecular oxygen was used for oxide growth, and the oxygen pressure was remotely controlled for engineering the Si/STO interface conditions. Prior to the growth, the silicon substrate was cleaned with 2% HF for 90 seconds right before introduction in ultra-high vacuum (UHV). The wafer was then transferred into the oxide MBE chamber with $5e^{-10}$ Torr base pressure. The substrate was first heated in UHV up to 700 ˚C, with the observation of (2x1) reconstruction monitored *in-situ* by reflection high-energy electron diffraction (RHEED). Next, ½ monolayer (ML) of Sr interfacial layer was evaporated to the silicon surface and controlled by RHEED with the stabilization of the (2x1) surface reconstruction from the ½ ML Sr-Si(001). Afterwards, the substrate was cooled down to 350 ˚C, for the direct epitaxy of $SrTiO_3$.

 The STO layers were then analyzed by high resolution X-ray diffraction (HR-XRD) and X-ray reflectometry (XRR) for their crystallinity and thickness. Detailed interface crystallinity was inspected by transmission electron microscopy (TEM) on a double corrected Titan[3] G2 60-300 (Thermo Fisher) instrument operating at 200 kV. For compositional analysis, Rutherford backscattering spectrometry (RBS) was used to investigate the stoichiometry (Sr/(Sr+Ti) ratio) in the perovskite layer, and the chemical binding status was explored by X-ray photoelectron spectroscopy (XPS). Optical property characterization was carried out by spectroscopic ellipsometry (SE) with a J. A. Woollam RC2, and the optical indices were fitted and extracted by using the CompleteEASE software. In addition, surface roughness was included when

analyzing the optical behaviors, and was measured by Bruker dimension edge atomic force microscopy (AFM).

Results and Discussion

The STO thin films are grown by co-deposition of strontium, titanium, and molecular oxygen. Since the pristine dimerized silicon surface is very reactive under oxygen ambient and forms amorphous SiO_x on its surface, the control of the SrO interfacial layer is extremely important to enable the epitaxy of the perovskite oxide. We therefore realized a series of experiments by controlling the molecular oxygen surface exposure expressed in Langmuir (1 L = $1e^{-6}$ Torr s) of the initial (2x1) Sr-Si(001) before to start the STO epitaxy. Different surface coverage with varied Langmuir values, ranging from 1.5 to 70, were used in our experimental plan. The Langmuir values (L) were extracted from the integrated pressure-time profile before opening the Sr and Ti shutters. Figure 1 summarizes the RHEED patterns along the $[110]_{STO}$ direction acquired after 1-nm and 4-nm growth of STO in function of molecular oxygen exposure. With limited oxygen exposure (1.5 L and 2 L), the STO layer grows directly on SrO/Si(001) as confirmed by the 2D streaks and low background intensity on the RHEED pattern from the early stage of the growth (Fig. 1(a) and (b)); on the other hand, with overexposure of molecular oxygen, an amorphous RHEED pattern was observed as shown in the Fig. 1(c). The crystallinity in the early stage largely impacted the subsequent growth, as the RHEED patterns after 4 nm of growth followed the initial behaviors (Fig. 1(d)-1(f)). In the Fig. 1 (d) and (e), a x2 surface reconstruction from Sr-rich surface was observed on RHEED pattern along the $[110]_{STO}$ direction. The compositional quantification was confirmed by RBS, with the Sr/(Sr+Ti) ratio larger than 0.5 for our STO samples (SI 1). The slight excess of Sr can result in more SrO,

which can promote the crystallization of STO according to the work of Saint-Girons et al, in which they argued that the $SrO/SrO/TiO_2$ stacking is more easily crystallized compared with normal SrO/TiO_2 stacking[13].

The interfacial layers were further inspected by cross-sectional TEM, as shown in the Figure 2. Both 1.5 L and 2 L samples showed single crystalline STO on top of Si substrate, with a very sharp and coherent interface. The ½ ML of Sr oxidized to SrO upon the oxygen exposure, which enabled the transition from the Si diamond structure to a perovskite structure with 45-degree rotation, reducing the lattice mismatch for the subsequent STO epitaxy. Compared with 1.5 L, the sample with 2 L exposure showed smoother transition with no dislocations or voids and pits in the interface, suggesting a more complete formation of SrO. With the well-controlled interface oxidation, the 4-nm STO was fully strained on Si from the FFT analysis of the TEM images (SI. 2). However, the over-exposure (> 2 L) led to an over oxidation of the SrO/Si interface which resulted into an amorphous STO layer. Compared with the crystalline STO, the 25 L sample showed very flat Si surface with no clear evidence of interfacial reactions, suggesting the amorphous layer was formed at the beginning of the growth process.

The STO chemical binding as well as STO/Si interface were investigated by XPS analysis. Besides different amount of exposure, an additional 1.5 L sample with high-temperature (580 ˚C) post-deposition annealing in the MBE chamber was also included in the analyses. The Si *2p* peaks of different growth condition samples were examined, as shown in the Figure 3(a). As expected, the intensity of the Si sub-oxides peak, located at 102 eV, raised as the exposure amount increased. For STO with low exposure amount, the sub-oxides peak intensity came from the Si-O-Sr interface. The additional post growth annealing at 580 ˚C showed very little impact on the peak intensity, demonstrating the high stability of interface in ultra-high

vacuum. On the contrary to the crystalline STO samples, the amorphous ones showed much higher Si sub-oxides intensity. This increase indicated larger amount of Si bonded to oxygen, suggesting the formation of thick SiO_x interfacial layer. With excess oxygen exposure prior to the growth of STO, the ½ ML Sr-Si surface was too thin to prevent the silicon surface oxidation, thus resulting into amorphous SiO_x and obstructed the epitaxial growth of STO.

The amorphous samples also showed different behavior in Ti and Sr XPS core peaks, as plotted in the Figure 3(b) and (c). In Fig. 3(b), the Ti intensity from the Ti *2p* core level largely decreased as the molecular oxygen exposure amount increased. This drop of intensity indicated the Sr/Ti ratio inside the STO films was not stable in function of oxygen exposure, and the films evolved to Sr-rich $SrTiO_3$ oxide. For the Sr *3d* core levels, presented in the Fig. 3(c), the shift to higher binding energy was clearly observed for the amorphous STO samples, which is attributed to the formation of $SrCO_x$ alloy[14,15]. This $SrCO_x$ was not formed inside the MBE chamber, but transformed from the amorphous Sr-rich oxides after the samples were exposed to air at atmospheric pressure[16].

To investigate the optical properties of different STO films, spectroscopic ellipsometry (SE) was used. To obtain better fittings and more accurate optical indices, we had measured at various incident angles ranging from 45˚ to 85˚; furthermore, the thickness of STO layer was determined by XRR and fixed to improve the fitting accuracy. Compared with TEM, the detecting area is larger for XRR, which can reduce the thickness error from local variations in ultra-thin films. The XRR curves were fitted with a two-layers model, and the extracted values were listed in the supporting information (SI. 3). In addition, the surface roughness of different samples by AFM were also measured (SI. 4), which could be applied to improve both the fitting accuracy of XRR and the subsequent SE analysis. In the fitting procedure of the SE

data, we used oscillator models for the individual films in order to ensure Kramers-Kronig consistency for relevant physical models. In the final results, all the SE fitting mean square errors were smaller than 5 by the CompleteEASE software[17], indicating the consistency between measured and simulated curves. The detailed SE fitting parameters and spectra are included in the supporting information (SI. 5).

All the SE spectra were fitted with two layers, and the optical indices of STO layers were extracted as shown in the Figure 4. In the Fig. 4(a), the real part of refractive index n was plotted from 250 nm to 800 nm wavelength, including all the visible light range. This wavelength range is important for optical and display applications such as video holography, thus requires a more detailed study. At 500 nm wavelength, the highest n in our STO film is 2.23, which was still smaller compared with the bulk value 2.48. The lowering of refractive index is common in thin film properties due to more defect and larger surface contributions[18]. In comparison with ultra-thin STO, we also measured a perfectly stoichiometric and highly crystalline 100-nm STO film on silicon also grown by MBE, which showed to have optical n values identical to the STO bulk reference. The impact of crystallinity was also compared with the thick amorphous STO layer (>1 μm) from literature which still showed n values smaller than our 4-nm epitaxial film[19]. In Fig. 4(a), it was obvious the crystalline and amorphous samples showed clear differences in n values, with crystalline samples having indices larger and closer to the reference values. Based on the XPS results, the amorphous samples became closer to $SrCO_x$ when the oxygen amount increased. This transformation was also observed when comparing with the theoretical n values of $SrCO_3$ and $SrTiO_3$. The n values of amorphous samples were in between these two values with 70 L sample even closer to $SrCO_3$, consolidating the interpretation of our XPS results.

Among the crystalline samples, the 2 L STO showed the highest n values while for the 1.5 L the refractive indices were lower with only marginal impact of the annealing. This difference indicated the 2 L sample having optical STO properties closer to the bulk ones, suggesting a certain amount of oxygen was needed in order to form a good interface and affect the quality of subsequent STO layer. Compared with the annealing, the interface control showed a stronger influence on the real part of the refractive index.

The extinction coefficient k is correlated to the absorption inside the material, which is directly linked to the bandgap energy. Since our STO film is only few nm thick, the reactive volume especially for the long wavelength is extremely small, making the determination of the k value rather difficult. As shown in the Figure 4(b), even though the k values obtained from SE fitting showed variations in slopes, the SE analysis, as used in this study, has no sensitivity for extinction coefficients below 0.01. The extinction coefficient values below 0.01 are extrapolations based on the model oscillators fitted in the spectral range with higher extinction coefficients. These oscillator values are also used to estimate a bandgap of the corresponding films from the extrapolation of the calculated absorption coefficients (SI. 6). For crystalline samples, the 1.5 L and 2 L samples showed similar slopes, with the extracted bandgap close to the theoretical value of SrTiO$_3$. For the 580 ˚C annealed STO, the slope was slightly sharper compared with the un-annealed ones, meaning the absorption was further reduced by annealing. On the other hand, the amorphous sample showed spectral shifts in the k values towards shorter wavelengths, indicating a larger bandgap inside the film. The theoretical bandgap of SrCO$_3$ is 4.4 eV[21,22], which suggests absorption below 280 nm. This value was consistent with the k profile we extracted for the amorphous 25 L sample.

With the control of oxygen exposure amount, we demonstrated the crystal quality of STO on Si(001) was largely impacted. In addition, Sr/Ti ratio inside STO film also varied as the oxygen pressure increased, resulting in different physical and optical properties. Based on the quantitative analyses results of RBS and XPS, we could calculate the relative sticking coefficient of Ti and Sr, as shown in the Figure 5(a). Both the sticking coefficients decreased when the oxygen amount was increased, but the Ti showed much largely impacted. For stoichiometric STO growth, both the Sr and Ti atomic fluxes required precise control. On the other hand, some perovskite oxides grown by MBE with volatile elements, such as Bi, Ru and Sn, showed to have totally different behavior[23–25]. These species possessed much smaller sticking coefficients due to large vapor pressure under high vacuum ambient. When growing oxides with these volatile species such as $BiFeO_3$, the overpressure of Bi as well as high oxygen pressure were used to form BiO_x to compensate the loss of Bi at high substrate temperature[26,27]. The differences in sticking coefficients resulted in different growth pattern of perovskite oxides and impacted the choice of substrates.

In our STO growth, the sticking coefficient decreased and the slope varied for different species. Compared to Sr, the oxide formation energy for Ti was much lower, as plotted in the Fig. 5(b)[28,29]. Thus, when excess oxygen was introduced into the MBE chamber, Ti atoms would be more easily oxidized into TiO_2. Due to the formation of TiO_2, less Ti participated in the formation of $SrTiO_3$, resulting in the lowering of sticking coefficient and the Sr-rich oxide film in the end.

Conclusion

10

Interface control is important for epitaxial films, and especially crucial for this oxide/Si system due to the easily formed SiO_x. By changing the gas exposure amount just before the STO growth, we could control the interface thickness and composition, leading to distinct differences of the STO films on top. With excess oxygen, the interface became amorphous and heavily oxidized, making the STO film amorphous as well; furthermore, the oxide films became non-stoichiometric due to oxidation of the metallic species, which also showed influence on the optical properties. The oxygen exposure showed to have an optimized amount to gently oxidized the ½ ML Sr, leading to smooth transition and the epitaxial growth, resulting in properties that were closer to the bulk ones. Finally, the post-annealing showed improvement on the film extinction behavior while kept the interface thin and unchanged. This further modification could be used to slightly adjust the optical behavior of the epitaxial thin films.

Acknowledgement

References

[1]   A. Kozyrev, A. Ivanov, A. Prudan, O. Soldatenkov, E. Hollmann, V. Loginov, D. Ginley, T. Rivkin, Microwave phase shifter employing srtio3 ferroelectric varactors, Integr. Ferroelectr. 24 (1999) 287–295.

https://doi.org/10.1080/10584589908215598.

[2]   M. Janousch, G.I. Meijer, U. Staub, B. Delley, S.F. Karg, B.P. Andreasson, Role of Oxygen Vacancies in Cr-Doped SrTiO3 for Resistance-Change Memory, Adv. Mater. 19 (2007) 2232–2235. https://doi.org/https://doi.org/10.1002/adma.200602915.

[3]   Z. Wang, M. Cao, Z. Yao, G. Li, Z. Song, W. Hu, H. Hao, H. Liu, Z. Yu, Effects of Sr/Ti ratio on the microstructure and energy storage properties of nonstoichiometric SrTiO3 ceramics, Ceram. Int. 40 (2014) 929–933. https://doi.org/https://doi.org/10.1016/j.ceramint.2013.06.088.

[4]   E. Mikheev, B.D. Hoskins, D.B. Strukov, S. Stemmer, Resistive switching and its suppression in Pt/Nb:SrTiO3 junctions, Nat. Commun. 5 (2014) 3990. https://doi.org/10.1038/ncomms4990.

[5]   D.G. Schlom, J.H. Haeni, A Thermodynamic Approach to Selecting Alternative Gate Dielectrics, MRS Bull. 27 (2002) 198–204. https://doi.org/DOI: 10.1557/mrs2002.71.

[6]   R.A. McKee, F.J. Walker, M.F. Chisholm, Crystalline Oxides on Silicon: The First Five Monolayers, Phys. Rev. Lett. 81 (1998) 3014–3017. https://doi.org/10.1103/PhysRevLett.81.3014.

[7]   R. Droopad, Z. Yu, H. Li, Y. Liang, C. Overgaard, A. Demkov, X. Zhang, K.

Moore, K. Eisenbeiser, M. Hu, J. Curless, J. Finder, Development of integrated heterostructures on silicon by MBE, J. Cryst. Growth. 251 (2003) 638–644. https://doi.org/https://doi.org/10.1016/S0022-0248(02)02200-5.

[8]   S. Abel, F. Eltes, J.E. Ortmann, A. Messner, P. Castera, T. Wagner, D. Urbonas, A. Rosa, A.M. Gutierrez, D. Tulli, P. Ma, B. Baeuerle, A. Josten, W. Heni, D. Caimi, L. Czornomaz, A.A. Demkov, J. Leuthold, P. Sanchis, J. Fompeyrine, Large Pockels effect in micro- and nanostructured barium titanate integrated on silicon, Nat. Mater. 18 (2019) 42–47. https://doi.org/10.1038/s41563-018-0208-0.

[9]   A. Petraru, J. Schubert, M. Schmid, C. Buchal, Ferroelectric BaTiO3 thin-film optical waveguide modulators, Appl. Phys. Lett. 81 (2002) 1375–1377. https://doi.org/10.1063/1.1498151.

[10]   M. Tyunina, J. Narkilahti, J. Levoska, D. Chvostova, A. Dejneka, V. Trepakov, V. Zelezny, Ultrathin {SrTiO}3films: epitaxy and optical properties, J. Phys. Condens. Matter. 21 (2009) 232203. https://doi.org/10.1088/0953-8984/21/23/232203.

[11]   A. Dejneka, M. Tyunina, J. Narkilahti, J. Levoska, D. Chvostova, L. Jastrabik, V.A. Trepakov, Tensile strain induced changes in the optical

spectra of SrTiO3 epitaxial thin films, Phys. Solid State. 52 (2010) 2082–2089. https://doi.org/10.1134/S1063783410100124.

[12] Y. Tian, C. Adamo, D.G. Schlom, K.S. Burch, Optical properties of SrTiO3 on silicon(100), Appl. Phys. Lett. 102 (2013) 41906. https://doi.org/10.1063/1.4789752.

[13] G. Saint-Girons, R. Bachelet, R. Moalla, B. Meunier, L. Louahadj, B. Canut, A. Carretero-Genevrier, J. Gazquez, P. Regreny, C. Botella, J. Penuelas, M.G. Silly, F. Sirotti, G. Grenet, Epitaxy of SrTiO3 on Silicon: The Knitting Machine Strategy, Chem. Mater. 28 (2016) 5347–5355. https://doi.org/10.1021/acs.chemmater.6b01260.

[14] F.V.E. Hensling, C. Baeumer, M.-A. Rose, F. Gunkel, R. Dittmann, SrTiO3 termination control: a method to tailor the oxygen exchange kinetics, Mater. Res. Lett. 8 (2020) 31–40. https://doi.org/10.1080/21663831.2019.1682705.

[15] A. Kosola, M. Putkonen, L.-S. Johansson, L. Niinistö, Effect of annealing in processing of strontium titanate thin films by ALD, Appl. Surf. Sci. 211 (2003) 102–112. https://doi.org/https://doi.org/10.1016/S0169-4332(03)00175-2.

[16] E. Bagherisereshki, J. Tran, F. Lei, N. AuYeung, Investigation into

SrO/SrCO3 for high temperature thermochemical energy storage, Sol.

Energy. 160 (2018) 85–93.

https://doi.org/https://doi.org/10.1016/j.solener.2017.11.073.

[17] I. J. A. Woollam Co., CompleteEASE Software Manual, (n.d.).

[18] S. Zollner, A.A. Demkov, R. Liu, P.L. Fejes, R.B. Gregory, P. Alluri, J.A.

Curless, Z. Yu, J. Ramdani, R. Droopad, T.E. Tiwald, J.N. Hilfiker, J.A.

Woollam, Optical properties of bulk and thin-film SrTiO3 on Si and Pt, J.

Vac. Sci. Technol. B Microelectron. Nanom. Struct. Process. Meas.

Phenom. 18 (2000) 2242–2254. https://doi.org/10.1116/1.1303741.

[19] Z. Wang, V. Kugler, U. Helmersson, E.K. Evangelou, N. Konofaos, S. Nakao,

P. Jin, Characteristics of SrTiO3 thin films deposited on Si by rf magnetron

sputtering at various substrate temperatures, Philos. Mag. B. 82 (2002)

891–903. https://doi.org/10.1080/13642810208218351.

[20] M. Wöhlecke, V. Marrello, A. Onton, Refractive index of BaTiO3 and

SrTiO3 films, J. Appl. Phys. 48 (1977) 1748–1750.

https://doi.org/10.1063/1.323822.

[21] Z. Hu, Y. Li, C. Zhang, B. Ao, Structural, electronic, optical and bonding

properties of strontianite, SrCO3: First-principles calculations, J. Phys.

Chem. Solids. 98 (2016) 65–70.

https://doi.org/https://doi.org/10.1016/j.jpcs.2016.06.009.

[22] Z. Ci, Y. Wang, Preparation, Electronic Structure, and Photoluminescence
      Properties of Eu2+-Activated Carbonate Sr1-xBaxCO3 for White Light-
      Emitting Diodes, J. Electrochem. Soc. 156 (2009) J267.
      https://doi.org/10.1149/1.3166183.

[23] A.B. Mei, Y. Tang, J. Schubert, D. Jena, H. (Grace) Xing, D.C. Ralph, D.G.
      Schlom, Self-assembly and properties of domain walls in BiFeO3 layers
      grown via molecular-beam epitaxy, APL Mater. 7 (2019) 71101.
      https://doi.org/10.1063/1.5103244.

[24] Z. Wang, H.P. Nair, G.C. Correa, J. Jeong, K. Lee, E.S. Kim, A.S. H., C.S. Lee,
      H.J. Lim, D.A. Muller, D.G. Schlom, Epitaxial integration and properties of
      SrRuO3 on silicon, APL Mater. 6 (2018) 86101.
      https://doi.org/10.1063/1.5041940.

[25] H. Paik, Z. Chen, E. Lochocki, A. Seidner H., A. Verma, N. Tanen, J. Park,
      M. Uchida, S. Shang, B.-C. Zhou, M. Brützam, R. Uecker, Z.-K. Liu, D. Jena,
      K.M. Shen, D.A. Muller, D.G. Schlom, Adsorption-controlled growth of La-
      doped BaSnO3 by molecular-beam epitaxy, APL Mater. 5 (2017) 116107.
      https://doi.org/10.1063/1.5001839.

[26] R.P. Laughlin, D.A. Currie, R. Contreras-Guererro, A. Dedigama, W.

Priyantha, R. Droopad, N. Theodoropoulou, P. Gao, X. Pan, Magnetic and

structural properties of BiFeO3 thin films grown epitaxially on SrTiO3/Si

substrates, J. Appl. Phys. 113 (2013) 17D919.

https://doi.org/10.1063/1.4796150.

[27] J.F. Ihlefeld, W. Tian, Z.-K. Liu, W.A. Doolittle, M. Bernhagen, P. Reiche, R.

Uecker, R. Ramesh, D.G. Schlom, Adsorption-Controlled Growth of $BiFeO_3$

by MBE and Integration with Wide Band Gap Semiconductors, IEEE Trans.

Ultrason. Ferroelectr. Freq. Control. 56 (2009) 1528–1533.

https://doi.org/10.1109/TUFFC.2009.1216.

[28] Y. Shen, Carbothermal synthesis of metal-functionalized nanostructures

for energy and environmental applications, J. Mater. Chem. A. 3 (2015)

13114–13188. https://doi.org/10.1039/C5TA01228G.

[29] D. Risold, B. Hallstedt, L.J. Gauckler, The strontium-oxygen system,

Calphad. 20 (1996) 353–361.

https://doi.org/https://doi.org/10.1016/S0364-5916(96)00037-5.

[30] J. Rams, A. Tejeda, J.M. Cabrera, Refractive indices of rutile as a function

of temperature and wavelength, J. Appl. Phys. 82 (1997) 994–997.

https://doi.org/10.1063/1.365938.

[31] M. Cardona, Optical Properties and Band Structure of SrTiO3 and BaTiO3,

Phys. Rev. 140 (1965) A651–A655.

https://doi.org/10.1103/PhysRev.140.A651.

[32] G.E. Pynchon, E.F. Sieckmann, Refractive Index of Strontium Oxide, Phys.

Rev. 143 (1966) 595–597. https://doi.org/10.1103/PhysRev.143.595.

Figure captions

Figure 1. RHEED patterns along [110]STO of (a)-(c) 1 nm STO and (d)-(f) 4 nm STO.

Figure 2. TEM cross-sectional images of (a) 1.5 L (b) 2 L and (c) 25 L samples. The 25 L sample showed to be amorphous.

Figure 3. XPS of (a) Si 2p peaks (b) Ti 2p peaks (c) Sr 3d peaks for different $SrTiO_3$ samples. The intensity of Ti and Sr is not normalized due to different amount presented in the samples.

Figure 4. Refractive indices (a) n values and (b) k values extracted by Ellipsometer fitting results. The reference values (dashed lines) are taken from literatures[10,21,30–32] The round and triangular points are respectively corresponding to the poly-crystalline and amorphous thick STO layers from references[19,20].

Figure 5. (a) Sticking coefficient of Sr and Ti based on RBS and XPS results in function of growth pressure. (b) formation energy for TiO_2 and SrO from references *Y. Shen, J. Mater. Chem. A, 2015 and D. Risold et al., Calphad, 1996*

Figure 1

1 nm SrTiO$_3$ 4 nm SrTiO$_3$
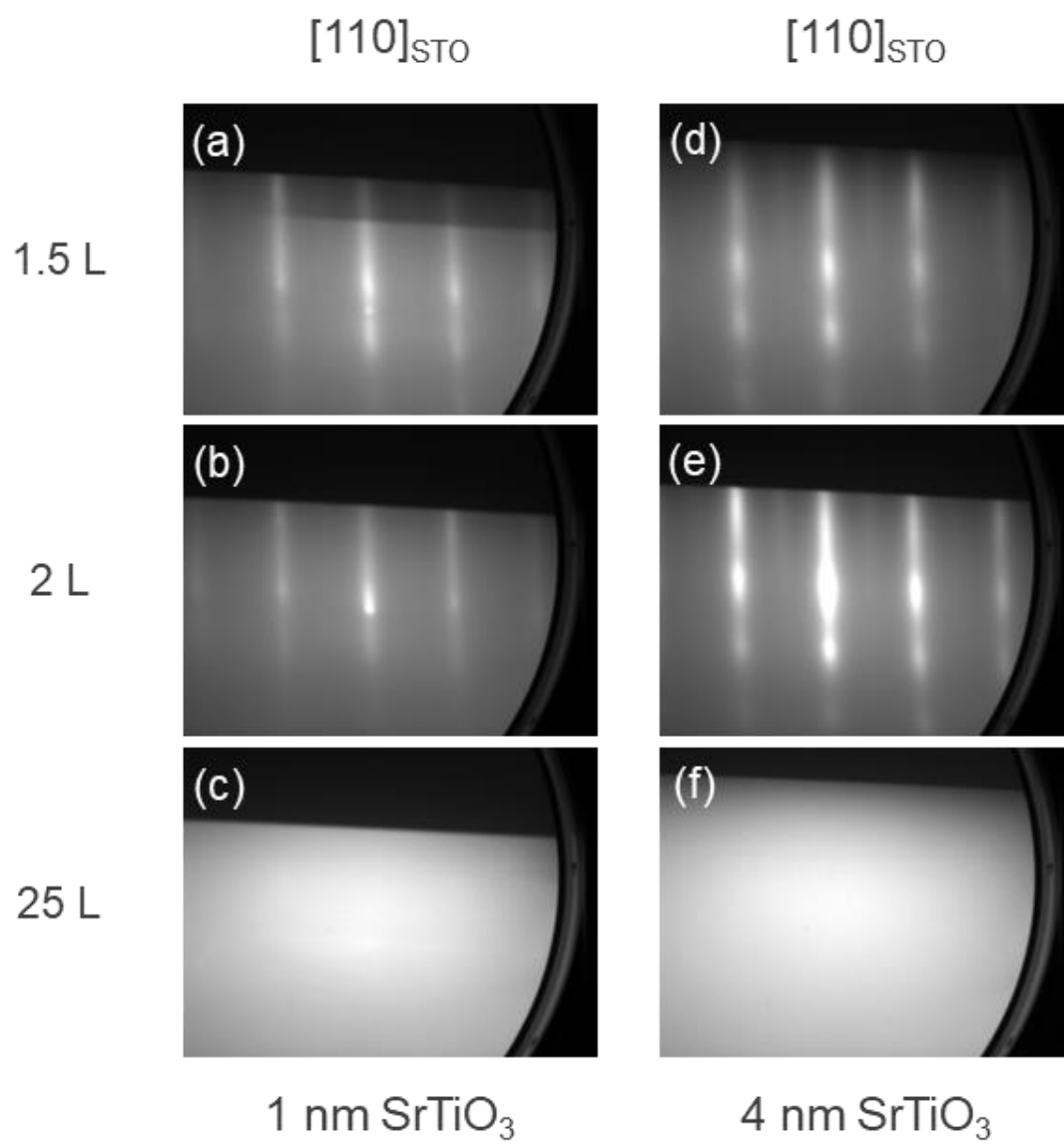
Figure 2
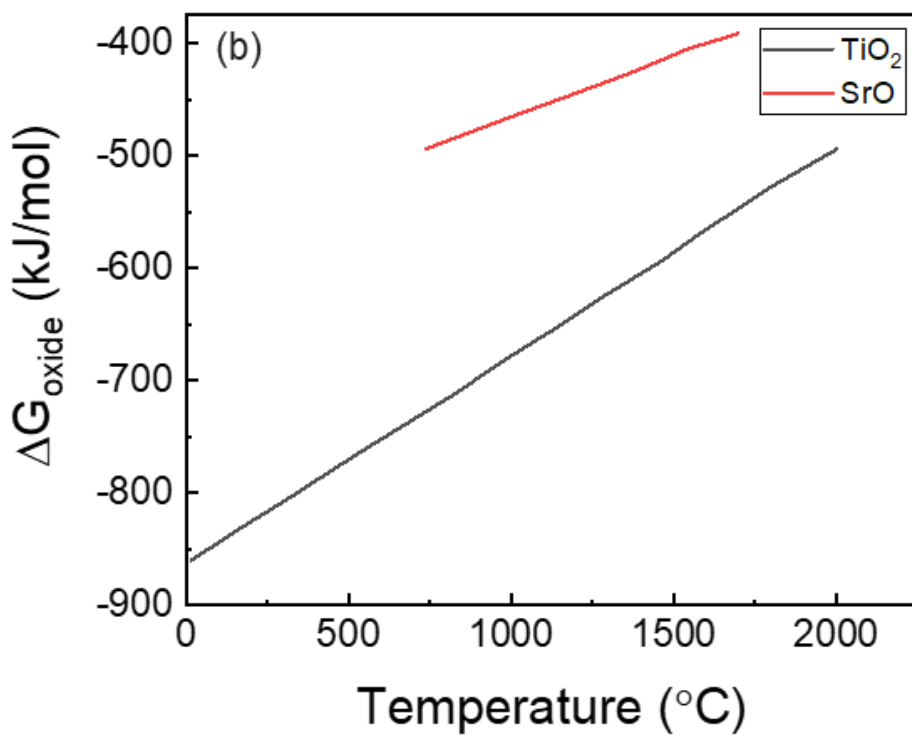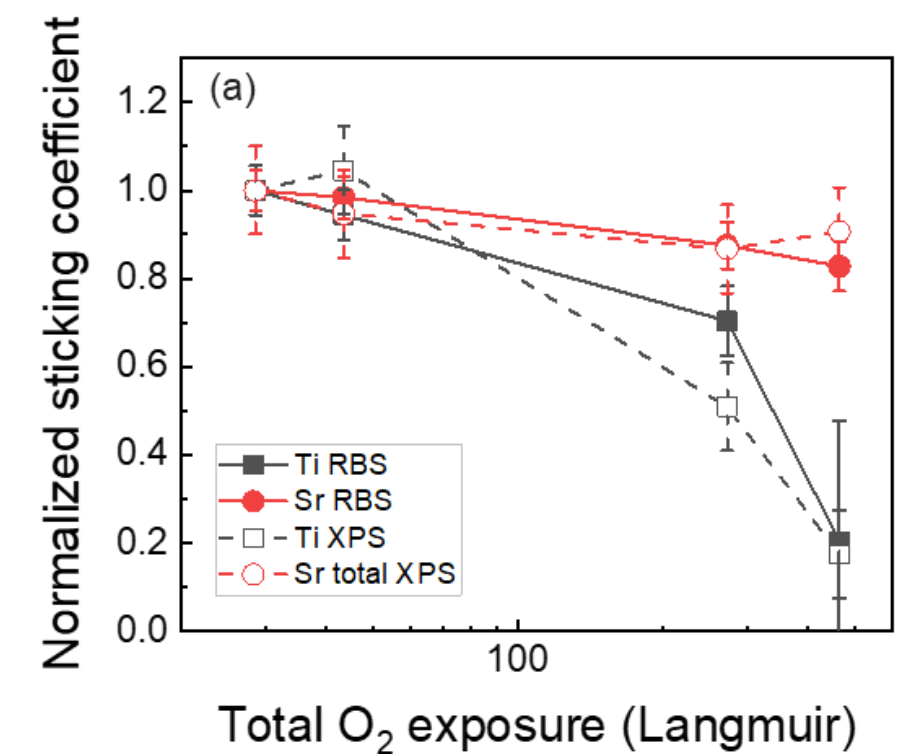
Figure 3

Figure 4

(a)

(b)
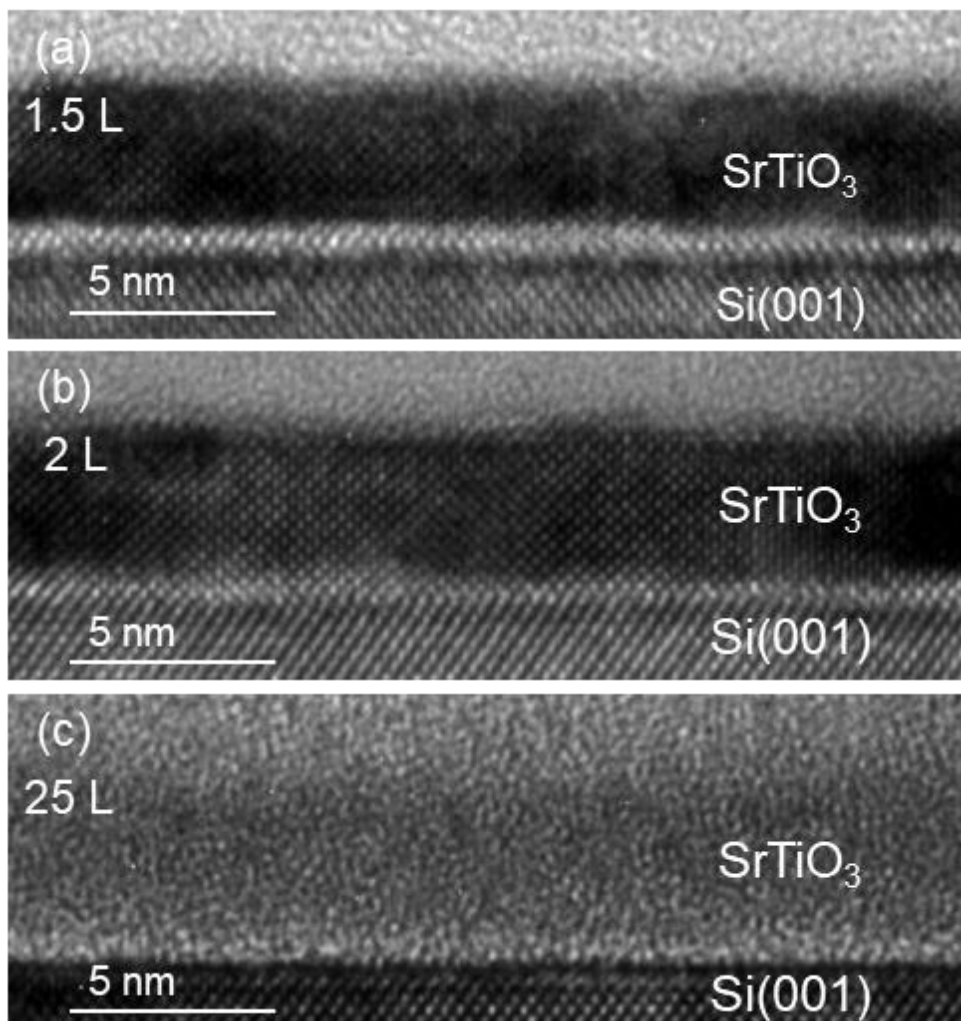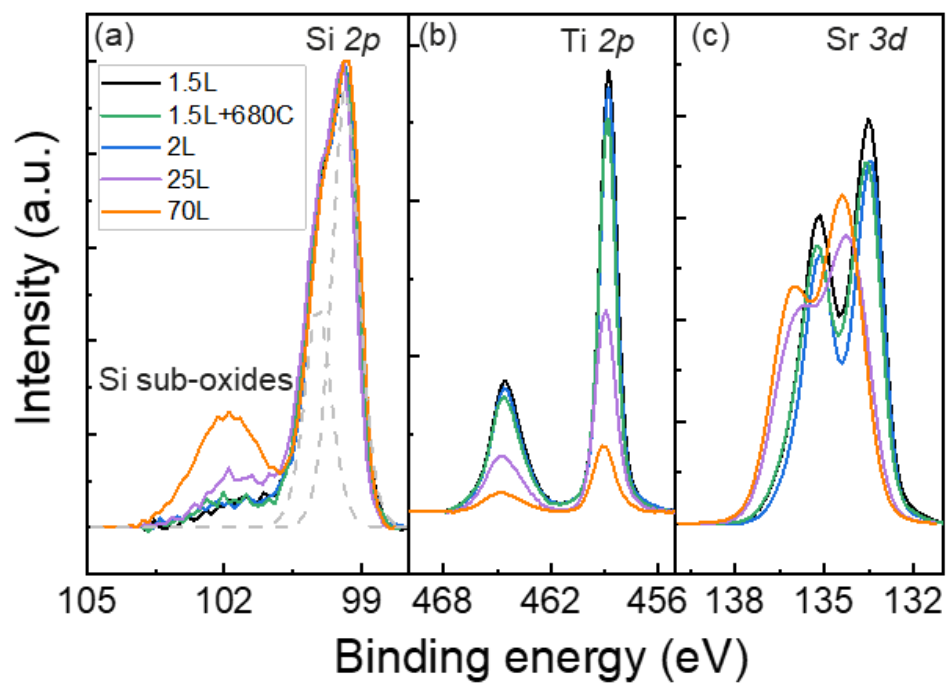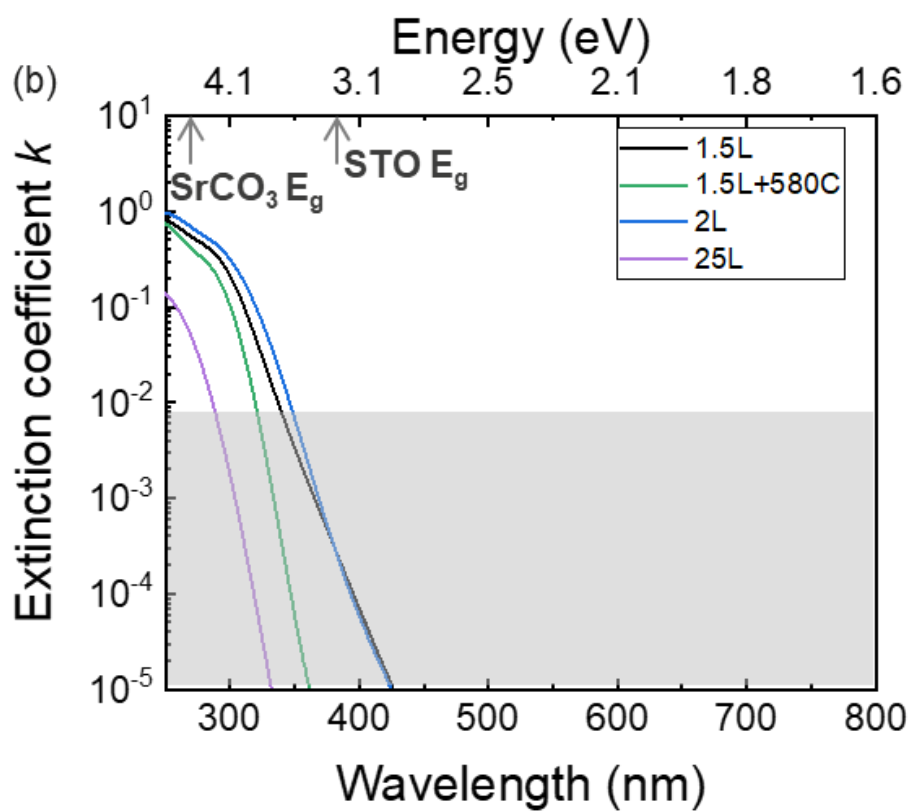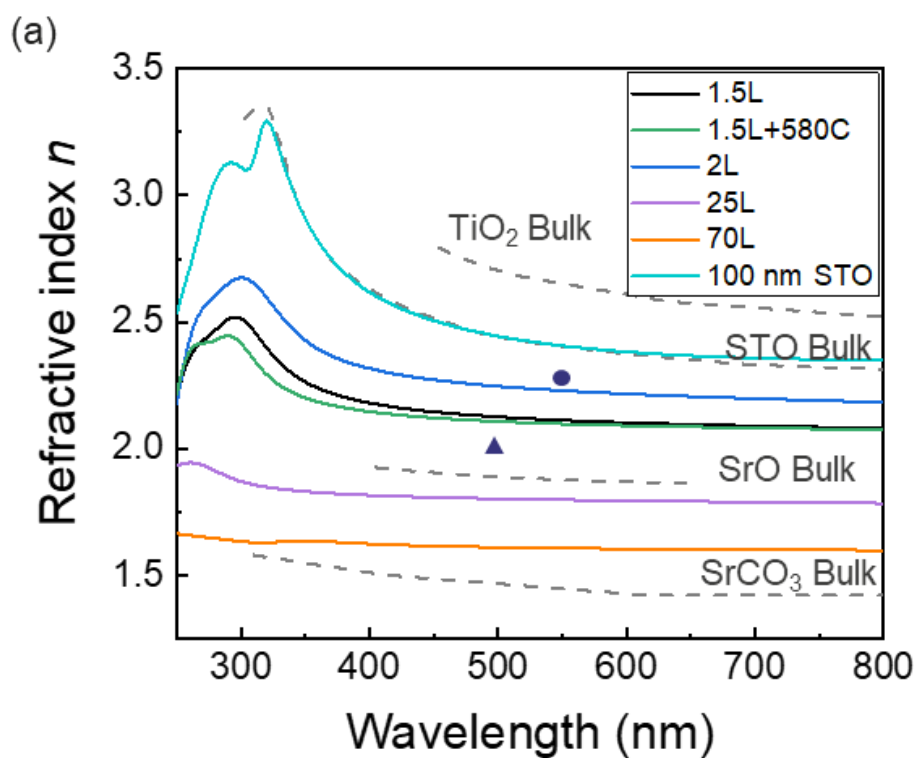
Figure 5

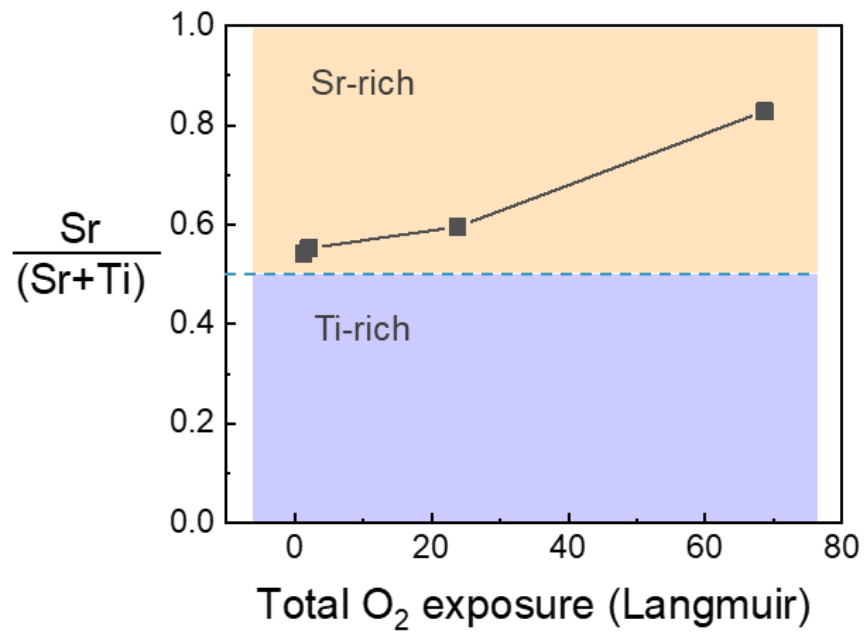**Supporting information**

SI 1
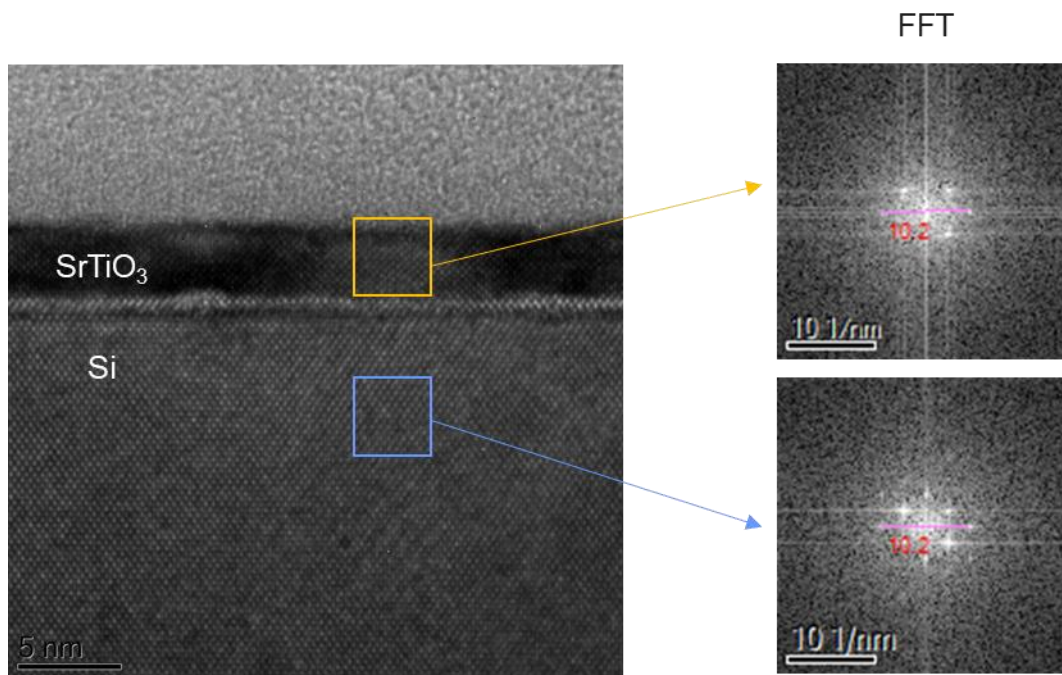

Figure S1. RBS results in function of Langmuir values.

SI 2

Figure S2. The FFT analysis of STO and Si layer.

Table S2. The extracted properties from XRR fitting results.

Layer	$d_{(220)}$
STO	0.196
Si	0.196

The measured distance in FFT images is the same for STO and Si layers, indicating a fully strained STO layer along the [110] direction.
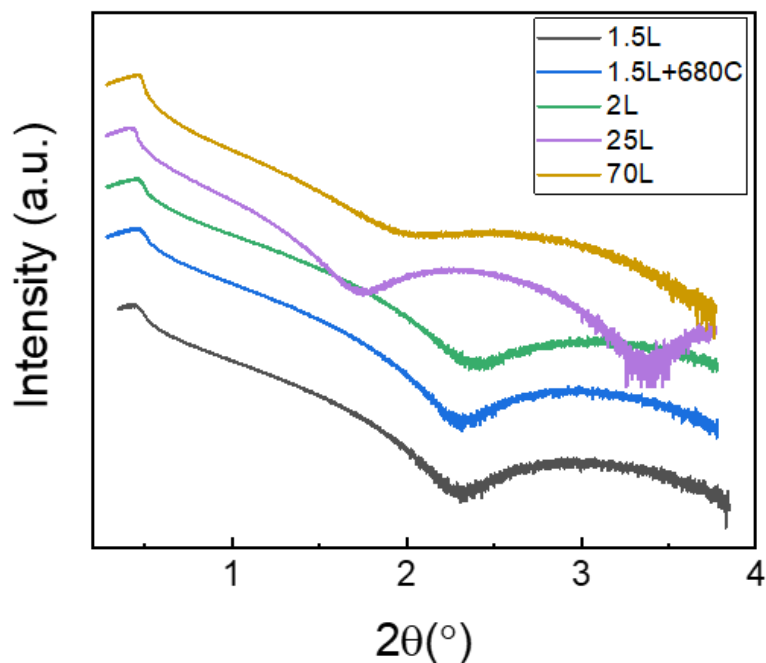
SI 3

Figure S3. XRR curves of different STO samples.

Table S3. The extracted properties from XRR fitting results.

Sample	STO thickness (nm)	Interface thickness (nm)	Surface roughness (nm)
1.5 L	4.31	0.63	0.09
2 L	4.27	0.56	0.30
25 L	5.54	0.72	0.16
70 L	4.94	1.32	0.16
1.5 L + 580C	4.06	0.88	0.14

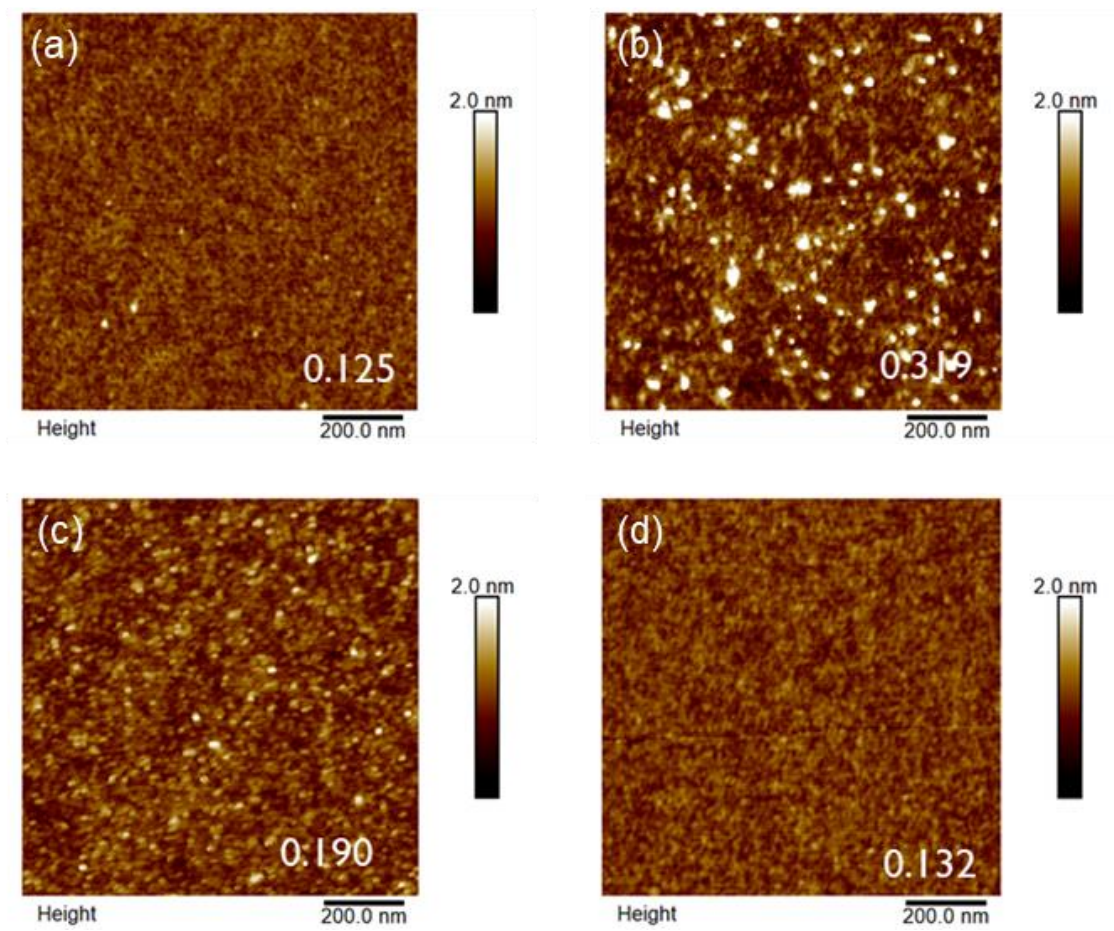The extracted thickness was used for the Ellipsometer fitting reference

SI 4

Figure S4. AFM of different STO samples. (a) 1.5 L (b) 2 L (c) 25 L (d) 1.5 L + 580 ˚C anneal

The obtained roughness is used for both XRR and Ellipsometry fitting model.
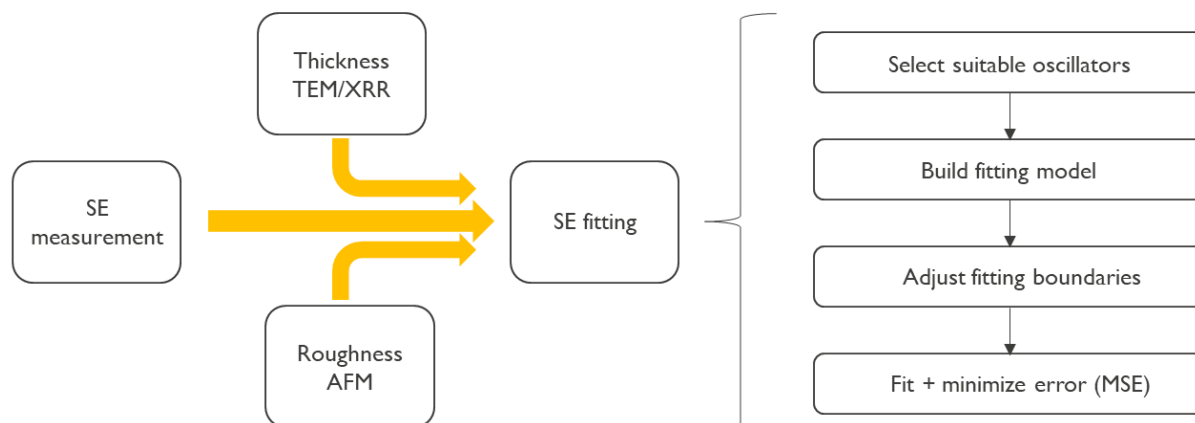
SI 5

Figure S5. Ellipsometry fitting procedure

To fit SE spectra, the thickness and roughness measured by other techniques are included to determine the starting point and fitting boundaries, which are crucial in order to have reliable results and not deviating from reality. In this fitting model, Gaussian oscillators are used to fit the absorption in short wavelength. All the fitting results are listed in Table S2 and the raw SE spectra with fitting curves are plotted in Figure S6.

Table S2. SE fitting results. All the fitted STO thickness are close to the XRR thickness with deviation no larger than 1.5%.

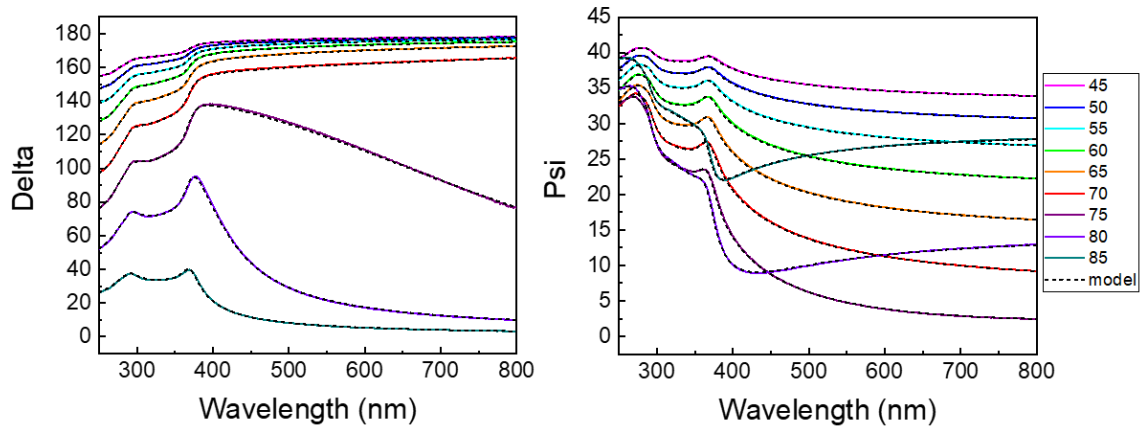| Sample	STO thickness (nm)	Interface thickness (nm)	Surface roughness (nm)	Fitting error MSE
1.5 L	4.34	0.69	0.18	4.233
2 L	4.19	0.65	0.38	4.295
25 L	5.47	0.89	0.21	4.350
70 L	5.16	1.31	0.05	4.611
1.5 L + 680C	4.08	1.04	0.28	4.468

Figure S6. Raw spectra of the 2 L sample. The dotted lines are produced by fitting model, which showed great consistency with raw spectra.

The MSE error values are calculated via the following equation by the CompleteEASE software[17]:

$$MSE = \sqrt{\frac{1}{3n - m} \sum_{i=1}^{n} \left[\left(\frac{N_{E_i} - N_{G_i}}{0.001} \right)^2 + \left(\frac{C_{E_i} - C_{G_i}}{0.001} \right)^2 + \left(\frac{S_{E_i} - S_{G_i}}{0.001} \right)^2 \right]}$$

where n is the number of wavelengths, m is the number of fit parameters, and $N = \cos(2\Psi)$, $C = \sin(2\Psi)\cos(\Delta)$, $S = \sin(2\Psi)\sin(\Delta)$. The measured data are subscripted with E and the model generated data are subscripted with G. The MSE value depends on not only the consistency between measured and model data, but also the complexity of film stacking. All our MSE values are smaller than 5, which indicated the deviation is small.

The correlation of STO refractive index n and the fitting model is examined by varying different thickness during the fitting procedure. The results including fitting error and change in n values are shown in Figure S7.
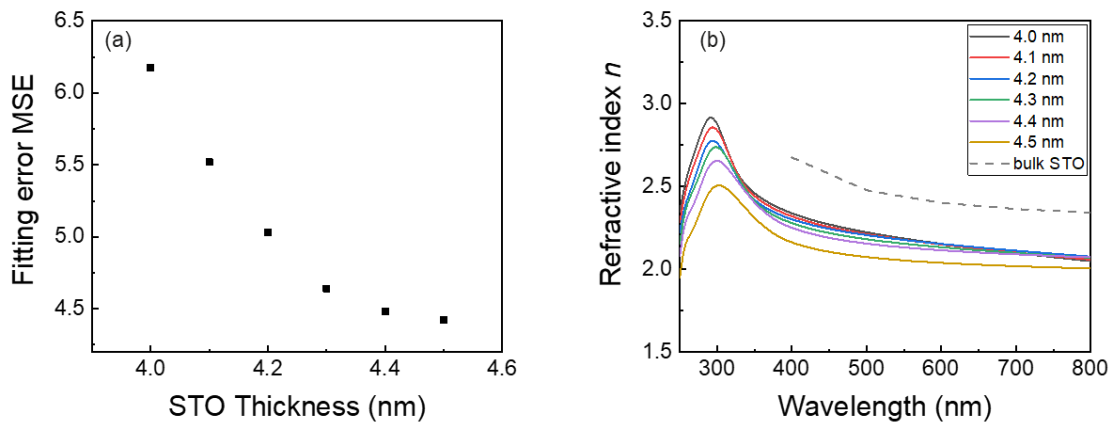
Figure S7. (a) MSE v.s. varied STO thickness (b) refractive index n when varying STO thickness

When thickness deviates from the real value obtained by XRR and TEM, the fitting error MSE increases rapidly. Meanwhile, the n values show ~7 % differences for 0.5 nm of thickness variation. These prove the importance of correct input and the high sensitivity of our SE model.
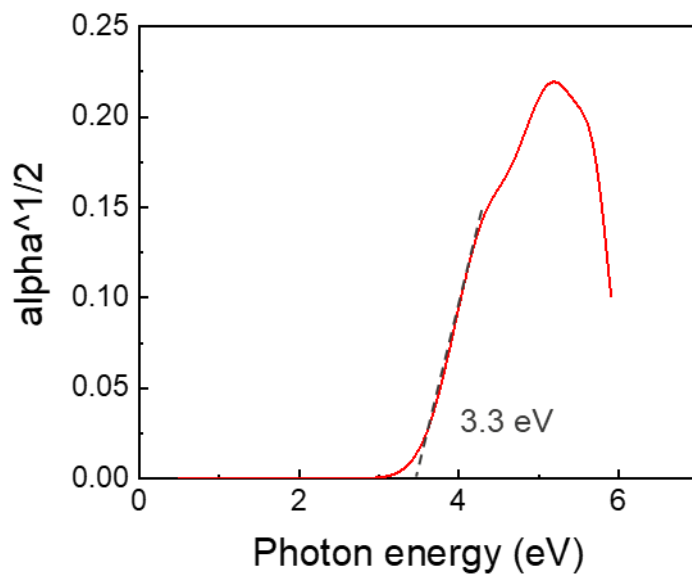
Figure S8. STO bandgap extrapolation

The bandgap of STO is extrapolated from the intercept of x-axis based on the graph of absorption coefficient v.s. photon energy. The absorption coefficient α is calculated from extinction coefficient k based on the equation

$$\alpha = \frac{4\pi k}{\lambda}$$